

IrO₂–SnO₂ mixtures as electrocatalysts for the oxygen reduction reaction in alkaline media

Cristina Locatelli · Alessandro Minguzzi ·
Alberto Vertova · Sandra Rondinini

Received: 11 September 2012 / Accepted: 22 December 2012 / Published online: 4 January 2013
© Springer Science+Business Media Dordrecht 2013

Abstract In this work, SnO₂ + IrO₂ mixed oxides are studied as electrocatalysts for the oxygen reduction reaction (ORR) in alkaline media by means of voltammetric techniques under controlled mass transfer conditions thanks to the use of rotating (ring) disk electrodes (RDE/RRDE). The oxides, prepared by sol–gel methodology, are supported on the disk electrodes using a thin layer of anionic exchange polymer as gluing agent. The amount of deposited polymer was optimized to avoid any limitation due to the diffusion of reactant/products across the film thickness. The mixed oxides were prepared at the following mole fractions of IrO₂: $x_{\text{IrO}_2} = 0.15, 0.31, 0.55, 0.73$, and 1. The role of composition was studied in terms of the reaction pathways and the relevant fraction of H₂O₂ production, together with the potentials of the onset of ORR. The fraction of sites able to give proton/hydroxyl and electron transfers is also determined and discussed. The results point to the best performance of low-Ir containing mixtures and to their low sensitivity to the presence of methanol, a key feature in the case of crossover in alkaline direct alcohol fuel cells.

Keywords Oxygen reduction · Direct alcohol fuel cells · Alkaline fuel cells · Iridium tin oxide · Rotating ring disk electrode

1 Introduction

In recent years, direct alcohol fuel cells (DAFCs) have been considered as more promising than the corresponding

H₂ fueled cells even for the highly demanding automotive industry, mainly because of their lower impact in terms of fuel storage, and of their high theoretical specific power (6 kW kg^{−1}) [1].

Nonetheless, the poisoning of the anode material, the slow kinetic of the oxygen reduction reaction (ORR) at the cathode and the energy loss connected with the alcohol crossover are still key factors that greatly affect the cell performance and limit the DAFCs development.

These aspects can be overcome by the correct selection of electrode materials. However, in acidic conditions, that is in cells based on proton conducting solid polymer electrolytes, the choice is limited to high cost-low available materials (e.g., Pt and its alloys).

More recently, the development of anion conducting membranes with the desired chemical and thermal stability in alkaline medium, paralleled by good ionic conductivity [2, 3], have made the adoption of alkaline working conditions realistic.

This in turn allows the improvement of ORR kinetics [4–6], and lowers the cathode cost since the research for suitable catalysts can be safely extended to non-noble metals and metal oxides. Among the families of non-noble transition metal oxides, particularly those based on Co, Fe, Cu, Mn [7–10], metal macrocycles [11, 12] offer the most promising properties.

In the present paper, the electrocatalytic activity of IrO₂–SnO₂ nanostructured mixed oxides toward ORR in alkaline condition is presented and discussed. The choice of Ir as the active component might appear contradictory with the need of low cost materials. However, we will demonstrate that the amount of Ir can be reduced to very low percentages while keeping (or even increasing) the catalytic activity.

In addition, thanks to the well-documented high activity of IrO₂-based materials towards the oxygen evolution

C. Locatelli · A. Minguzzi (✉) · A. Vertova · S. Rondinini
Dipartimento di Chimica, Università degli Studi di Milano,
Via Golgi 19, 20133 Milan, Italy
e-mail: alessandro.minguzzi@unimi.it

reaction (OER, water oxidation), this study gains interest in view of the development of reversible electrocatalysts, i.e., electrode materials that are able to catalyze both ORR and OER. Catalysts with these properties are particularly interesting in view of their use in Unitized Reversible Fuel Cells (URFCs), which combine the electrolyzer and the fuel cell functions.

The promising properties of IrO_2 as catalyst for the ORR have already been introduced [13–16]. However, a detailed study that includes the role of composition, the alcohol tolerance and the reaction paths/products (presence of hydrogen peroxide) is, to the authors' best knowledge, still missing and represents the aim of the present paper.

In order to maximize the catalytic activity/cost ratio, a careful design and control of morphology, bulk and surface features of the material is needed [17, 21].

Electrocatalytic materials in which the IrO_2 is dispersed in a less costly metal oxide (SnO_2) as matrix are obtained by sol–gel synthesis that allow to control the phase composition of the dispersed material, together with the possible surface segregation of the different components, and its morphology, i.e., the particle shape and size. In particular, after the encouraging results obtained in the case of binary mixtures as catalysts for the OER [17, 18], we adopted the impregnation method to ensure a complex but efficient distribution of the active material (IrO_2) on the top and within the diluting species (SnO_2) nanoparticles [18]. In addition, it will be shown that SnO_2 does not represent a mere supporting/diluting agent but leads to low-Ir content composites that show higher performances than pure IrO_2 .

The evaluation of the catalyst performance and specifically of the effect of the Ir content on ORR activity is presented and discussed in terms of kinetic current, percentage of peroxide ion production, and methanol tolerance.

2 Experimental

All the chemicals were of reagent grade purity and were used without further purification; doubly distilled water passed through a Milli-Q[®] apparatus was used to prepare solutions and suspensions.

2.1 Sample preparation

The electrocatalytic materials characterized in the present study are $\text{SnO}_2 + \text{IrO}_2$ mixed oxides at molar fractions $x_{\text{IrO}_2} = 0.15, 0.31, 0.50, 0.73, 1$. The different mixtures are denoted by adding the IrO_2 molar fraction in brackets: $\text{SnO}_2 + \text{IrO}_2 (x)$.

The $\text{IrO}_2 + \text{SnO}_2$ mixed oxides and SnO_2 nanoparticles were synthesized by sol–gel reaction at 25 °C as previously

reported in [19–21] starting from $\text{Sn}(\text{C}_4\text{H}_9\text{O})_4$ (Aldrich 99.999 %) and $\text{IrCl}_3 \cdot 3\text{H}_2\text{O}$ (Alfa Aesar 99.9 %).

$\text{IrO}_2\text{--SnO}_2$ mixed oxides are obtained by impregnation of the tin xerogel with an alcoholic solution of iridium trichloride. The dried xerogel is subsequently thermally treated under oxygen flow (50 Nl h^{-1}) at 450 °C for 2 h, after 3 h temperature ramp.

The powder was supported on the Glassy Carbon (GC) disk of the rotating disk electrode (RDE) or rotating ring disk electrode (RRDE). Before use the GC surface (geometric area: RDE 0.196 cm^2 ; RRDE 0.126 cm^2) was polished with Al_2O_3 abrasive powder ($0.05 \mu\text{m}$) and rinsed in an ultrasound bath with water and acetone for 2 min each. Before the deposition of a fresh aliquot of powder, the cleanness of the GC was verified by cyclic voltammetry.

The electrodes were prepared by transferring with a micropipette aliquots of 10–20 μL of the aqueous suspension, previously immersed for 2 min in an ultrasonic bath, to attain the desired powder loading. The concentrations of the suspensions are: 7 mg mL^{-1} for $\text{SnO}_2 + \text{IrO}_2 (0.15)$, 6.5 mg mL^{-1} for $\text{SnO}_2 + \text{IrO}_2 (0.31)$, 4 mg mL^{-1} for $\text{SnO}_2 + \text{IrO}_2 (0.50)$, 3 mg mL^{-1} for $\text{SnO}_2 + \text{IrO}_2 (0.73)$, and 3.5 mg mL^{-1} for IrO_2 . The electrode loadings were reported in terms of weight of metal per geometric area (mg cm^{-2}).

After water evaporation under forced hot air flow, aliquots of 2–5 μL of an appropriate dilution of the as received suspension of the polymeric anionic membrane (PAM, 5 wt% Tokuyama[®] in isopropanol) were added in order to obtain a good adhesion of the catalyst layer to the support surface. The dilution ratio was adjusted in order to keep the ratio of 70 (mg deposited powder)/(mg dry polymer), see Sect. 3, and to limit the volume of the addition to 2–5 μL .

2.2 Electrochemical characterization

All the electrochemical measurements were carried out at 25 °C in a 3-electrode cell using NaOH 0.1 M as electrolyte. Modified RDE and RRDE were used as working electrodes and a graphite rod was used as counter. Even if the aqueous saturated calomel electrode (SCE) was used as reference electrode, all potentials are here referred to the reversible hydrogen electrode (RHE) by periodical calibration of SCE.

The kinetic activity of these electrocatalytic materials toward ORR was evaluated by cyclic voltammetry (CV) and staircase voltammetry (SV). CVs were recorded between 1.4 and 0.4 V vs RHE at 20 mV s^{-1} . SVs were recorded between 1.1 and 0.1 V vs RHE, each voltage step having 10 mV amplitude and 10 s length, to attain quasi-steady-state conditions.

All measurements were first performed in N_2 -saturated and subsequently in O_2 -saturated solutions, at different

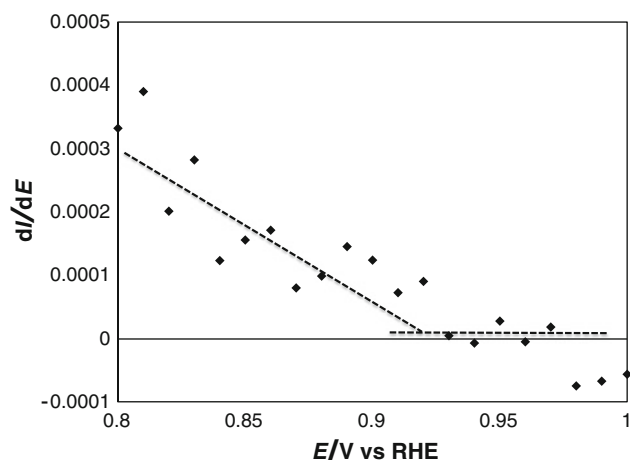


Fig. 1 dI/dE behavior of $\text{SnO}_2 + \text{IrO}_2$ (0.31) on RRDE in 0.1 M NaOH O_2 -saturated. The E_{ORR} values is determined in the intersection of the two straight lines

rotation rates (400, 900, 1600, 2500 rpm). All the SV curves reported here were obtained by subtracting the polarization curve recorded under N_2 atmosphere to the one recorded in the presence of O_2 at the same rotation rate. After each run the stability of the material and of the deposit were checked under CV conditions at 2500 rpm in the presence of O_2 .

Electrochemical measurements on RDE electrode were recorded using a Solartron 1287A Potentiostat/Galvanostat driven by Corrware[®] (Scribner Associates Inc). Measurements performed on the RRDE (RRDE-3A Biologic Science Instrumentation, glassy carbon disk, Au ring) were recorded by a bipotentiostat (CH Instruments, 920C). The Au ring was set at 1.3 V (RHE) to oxidize the hydrogen possibly produced at the disk. The ring collection efficiency, N , is determined at the end of each measurements in 2 mM $\text{K}_3[\text{Fe}(\text{CN})_6]$ in aqueous 0.1 M KNO_3 .

E_{ORR} , the ORR onset potential, i.e. the potential value at which the ORR starts, is determined considering the dI/dE versus E (RHE) characteristics (an example is reported in Fig. 1). The intersection point between the two straight lines gives the E_{ORR} value.

3 Results and discussion

Table 1 reports the four IrO_2 – SnO_2 mixed oxides discussed in this work, together with the S_{BET} ($\text{m}^2 \text{g}^{-1}$) surface areas, and the surface Ir/Sn atomic ratio obtained by the XPS analysis [22]. The nominal values, in column 5, are added for the sake of comparison.

Data of S_{BET} show a monotone decrease at increasing IrO_2 content, and XPS results show the parallel Ir

Table 1 Surface areas and the Ir/Sn ratio for all the $\text{SnO}_2 + \text{IrO}_2$ investigated

#	Composition	$S_{\text{BET}}/\text{m}^2 \text{g}^{-1}$	Ir/Sn surface	Ir/Sn nominal
1	$\text{SnO}_2 + \text{IrO}_2$ (0.15)	77.4	1.76	0.18
2	$\text{SnO}_2 + \text{IrO}_2$ (0.31)	53.7	46.6	0.45
3	$\text{SnO}_2 + \text{IrO}_2$ (0.50)	19.8	58	1.00
4	$\text{SnO}_2 + \text{IrO}_2$ (0.73)	9.5	∞	2.70

enrichment at the surface. This is correlated to the method of Ir precursor addition. As reported in [18] the impregnation method allows to obtain materials with the highest surface concentration of the active material. This might be attributed to the progressive growth of iridium oxide over the tin xerogel particles, which ultimately gives rise to larger agglomerates. This is particularly evident at the highest Ir content so that in sample 4 only Ir species are localized at the surface.

Figure 2 collects the X-ray diffraction lines of samples 1–4, calcined at 450 °C. Reference spectra of pure IrO_2 and SnO_2 are reported for comparison.

The vertical lines highlight the peak positions of the same hkl planes for the structurally isomorph tin (dotted lines) and iridium (dashed lines) oxides.

At increasing IrO_2 content the characteristic peaks progressively broaden and shift, being the sum of the two different contributions (IrO_2 and SnO_2). The shift of the main peak (110 plane) from 26.7° to 28.8° is due to the increasing prevalence of IrO_2 phase. In particular, in the case of

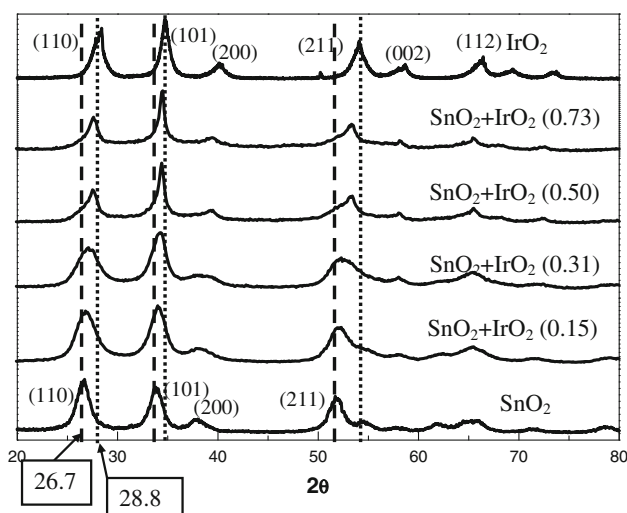


Fig. 2 X-ray diffractograms of $\text{SnO}_2 + \text{IrO}_2$ powders. The vertical lines indicate the peak positions for the pure oxides: dotted line for IrO_2 and dashed line for SnO_2 [22]

materials with higher Ir/Sn molar ratio ($\text{SnO}_2 + \text{IrO}_2$ (0.73), $\text{SnO}_2 + \text{IrO}_2$ (0.50)), the characteristic peaks are close to those shown by pure IrO_2 but the broad shoulder observed between 2θ 52° and 53° is likely due to the decreasing contribution of SnO_2 . This is in line with the results reported in [17, 18] that show that the impregnation method leads to materials with a small amount of segregated IrO_2 phase.

These samples were characterized under oxygen reduction conditions by means of the RRDE, which sums up the control of the mass transport rate of reactants/products to/from the electrode surface, like the RDE device, and the possibility of shedding light on the reaction mechanism by determining, at the ring, a selected reaction intermediate. It is therefore a unique tool for elucidating the pathway(s) of the ORR, and specifically for discriminating between the direct 4-electrons reduction and the sequence of two 2-electrons steps accompanied by the formation hydrogen peroxide as detectable intermediate, according to the following scheme:

A: “direct pathway”, 4-electron reduction	B: “peroxide pathway”, 2-electron reductions
$\text{O}_2 + 2\text{H}_2\text{O} + 4\text{e}^- \rightarrow 4\text{OH}^-$ (A1)	$\text{O}_2 + \text{H}_2\text{O} + 2\text{e}^- \rightarrow \text{OH}^- + \text{HO}_2^-$ (B1) $\text{HO}_2^- + \text{H}_2\text{O} + 2\text{e}^- \rightarrow 3\text{OH}^-$ (B2)

In turn, HO_2^- , formed in step B1, can disproportionate according to reaction (1):



It is evident that the A1 path is preferred for both energetic reasons and stability of the structural FC materials. Given the high corrosive properties of the peroxide ion, an electrode material able either to catalyze the direct pathway, thus preventing the peroxide ion formation, or to facilitate its rapid decomposition is a good candidate as cathode in low temperature fuel cell devices.

As described in Sect. 2, the RDE/RRDE were modified by transferring on the disk a known amount of the aqueous suspension of the selected powder. A drop of an alcoholic suspension of PAM is finally added to obtain a perfect adhesion of the powder on the support.

The PAM loading, w_{PAM} ($\mu\text{g cm}^{-2}$), was preliminary determined to avoid the onset of a diffusive contribution in the transport of the reactant/products across the polymeric film [23–25], while keeping its function of adhesive layer.

Figure 3 reports the SV curves recorded in oxygen saturated NaOH 0.1 M, at 2500 rpm, on the RRDE modified with the $\text{SnO}_2 + \text{IrO}_2$ (0.15) powder (electrode loading: 0.3 mg cm^{-2} of Ir) for different PAM loadings: namely, 10, 20, 40, $100 \mu\text{g cm}^{-2}$.

As can be observed, the potential of the ORR onset, $\sim 0.9 \text{ V}$ (RHE), is not influenced by the PAM layer. Vice

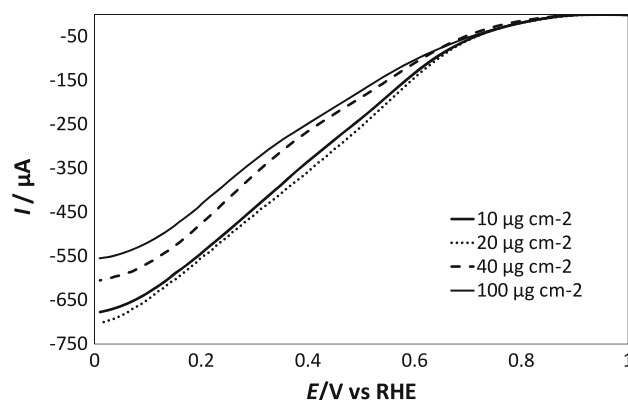


Fig. 3 Effect of the PAM loading on SV curves recorded on $\text{SnO}_2 + \text{IrO}_2$ (0.15) in O_2 -saturated 0.1 M NaOH at 2500 rpm

versa, the current intensity strongly depends on the PAM content, and markedly decreases when increasing the loading from 20 to $100 \mu\text{g cm}^{-2}$. This outcome is certainly bound to the increase of the film thickness, that slows down the diffusion of O_2 , solvent and hydroxyl ions to/from the catalytic layer. This effect can be quantified by analyzing the dependence of the reduction current on the rotation rate, for the different PAM loadings.

In fact, the total ORR current density at any RDE can be subdivided into kinetic, j_k , and mass transfer components. In the present case, to the usual transport term in solution, j_d , which depends on the square root of the angular velocity, an additional contribution has to be considered, j_f , which originates from the transport within the polymeric film and is independent from the rotation rate.

Summing up the three contributions, one obtains:

$$\frac{1}{j_L} = \frac{1}{j_k} + \frac{1}{j_d} + \frac{1}{j_f} \quad (2)$$

In particular:

$$j_d = 0.62nFD_{\text{O}_2}^{2/3}v^{-1/6}c_0\omega^{1/2} = nBc_0\omega^{1/2}, \quad (2a)$$

where D_{O_2} is the O_2 diffusion coefficient ($\text{cm}^2 \text{ s}^{-1}$), v is the kinematic viscosity of the solution ($\text{cm}^2 \text{ s}^{-1}$), c_0 is the O_2 bulk concentration in the electrolyte solution (mol cm^{-3}), and ω is the angular velocity (rad s^{-1}). Considering the solubility of molecular oxygen in NaOH 0.1 M at 25°C , the theoretical value of Bc_0 is equal to $1.3 \times 10^{-5} \text{ C s}^{-1/2}$;

$$j_f = nFc_fD_fL^{-1}, \quad (2b)$$

where L is the film thickness (cm), and c_f and D_f are the concentration and the diffusion coefficient of O_2 in the polymeric layer, respectively.

Under limiting conditions, the Koutecký–Levich plots obtained with RRDE having different PAM loadings are reported in Fig. 4.

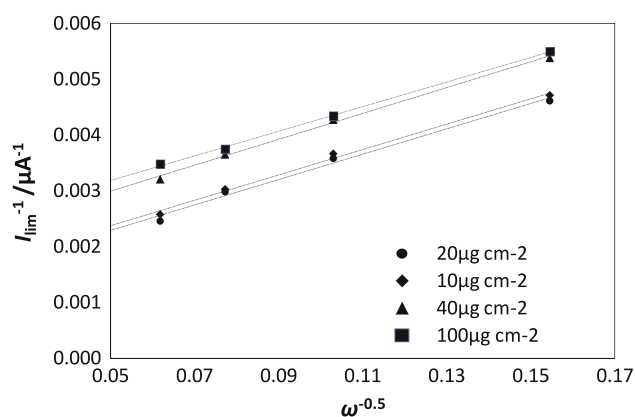


Fig. 4 Effect of the PAM loading on Koutecky–Levich plots at 0.35 V on $\text{SnO}_2 + \text{IrO}_2$ (0.15)

Four parallel straight lines are obtained, whose slope, according to the Eqs. (2) and (2a), corresponds to $(nBc_0)^{-1}$.

The intercept, $Y = \frac{1}{j_k} + \frac{1}{j_f}$, correlated to the thickness of polymeric film, L , and to the kinetic current, j_k , can be conveniently rearranged as:

$$\frac{1}{Y} = \frac{1}{(1/j_k) + (nFD_f C_f)^{-1} \cdot L} \quad (3)$$

For $L \rightarrow \infty$, high reactant diffusion resistance through the polymer electrolyte film, $1/Y \rightarrow 0$ and $Y \rightarrow \infty$.

For $L \rightarrow 0$, low reactant diffusion resistance through the polymer electrolyte film, $1/Y \rightarrow j_k$, and $Y \rightarrow 1/j_k$.

Since the PAM loading on the electrode is proportional to the film thickness, by plotting $1/Y$ versus w_{PAM}^{-1} one obtains the trend reported in Fig. 5.

At low $1/w_{\text{PAM}}$ values, that is at high film thicknesses, $1/Y$ is low, and increases with $1/w_{\text{PAM}}$ until, at $w_{\text{PAM}} \leq 20 \mu\text{g cm}^{-2}$, $1/Y$ reaches a plateau corresponding to j_k . This polymer loading corresponds to a ratio of 70 (mg/mg) between the weight of powder and the one of the

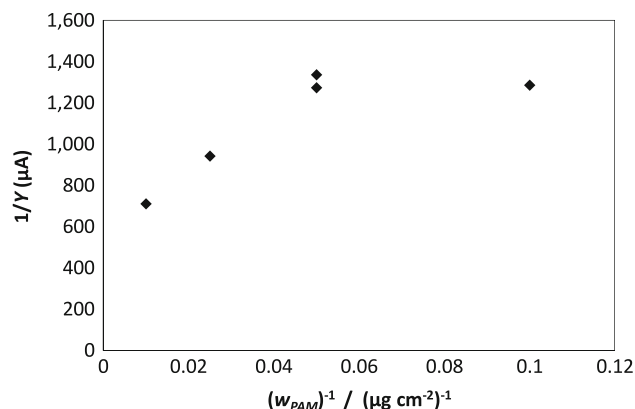


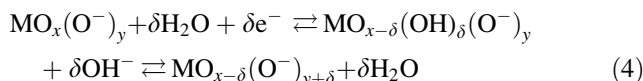
Fig. 5 Dependence of Koutecky–Levich intercept on the PAM loading

Tokuyama® dry polymer. This ratio is kept constant for all the investigated electrodes.

3.1 Electrocatalytical activity of IrO_2 – SnO_2 powders toward ORR

Figure 6 shows the CV of the mixed oxide, recorded between 1.4 and 0.4 V vs RHE, for different IrO_2 content, in aqueous 0.1 M NaOH saturated with N_2 (dotted line) or O_2 (solid line).

In this potential window and under N_2 -atmosphere, the Ir-based electrocatalysts show a typical pseudo-capacitive behavior according to the following equation [26, 27]:



The exchange of $\text{H}_2\text{O}/\text{H}^+/\text{OH}^-$ between the iridium active sites and the aqueous phase, accompanied by the electron transfer within the oxide phase, is at the basis of the “bumps” observed in the CVs.

At increasing IrO_2 mol fraction the bumps are shifted toward less positive potentials and the voltammetric charge, Q (mC), obtained by integration of each curve between 0.4 and 1.3 V, decreases (see Fig. 7). Since the Ir loading is fixed at 0.5 mg cm^{-2} , this latter effect is strictly bound to the decrease of the fraction of sites effectively used for the pseudo-capacitive reactions [17].

In fact, the voltammetric charge is an extensive parameter [19–21, 28, 29], representative of the total number of “available” sites, that is the sites able to exchange protons (or, as in this case, hydroxyl ions) with the solution [17, 30]. The actual fraction of the total Ir present in the mixtures, i.e., the nominal Ir content, is indicated in Fig. 7 at the corresponding x_{IrO_2} .

Note that this fraction results independent on the powder loading, as evidenced by the linear correlation between Q ($@ 20 \text{ mV s}^{-1}$) and the Ir loading obtained for $\text{SnO}_2 + \text{IrO}_2$ (0.15), as reported in Fig. 8.

The resulting straight line ($R^2 = 0.998$, slope = $0.0289 \text{ C cm}^2 \text{ mg}^{-1}$) gives a value of the usage of the iridium content (12.7 %) comparable with the single datum reported in Fig. 7 and with the average value obtained with the quantitative rapid screening methodology described in [17]. This result, besides demonstrating the effectiveness and reliability of the preparation procedure of the RDE electrodes, confirms that the diffusion of OH^- is not limited by the thickness of the polymer electrolyte layer.

In the O_2 -saturated electrolyte (Fig. 6a–e, full lines) an additional reductive current is visible, that is absent in the case of saturation with N_2 . The current intensity bound to ORR at the less positive potentials increases from 0.15 to 0.31 IrO_2 molar fraction, then starts to decrease toward

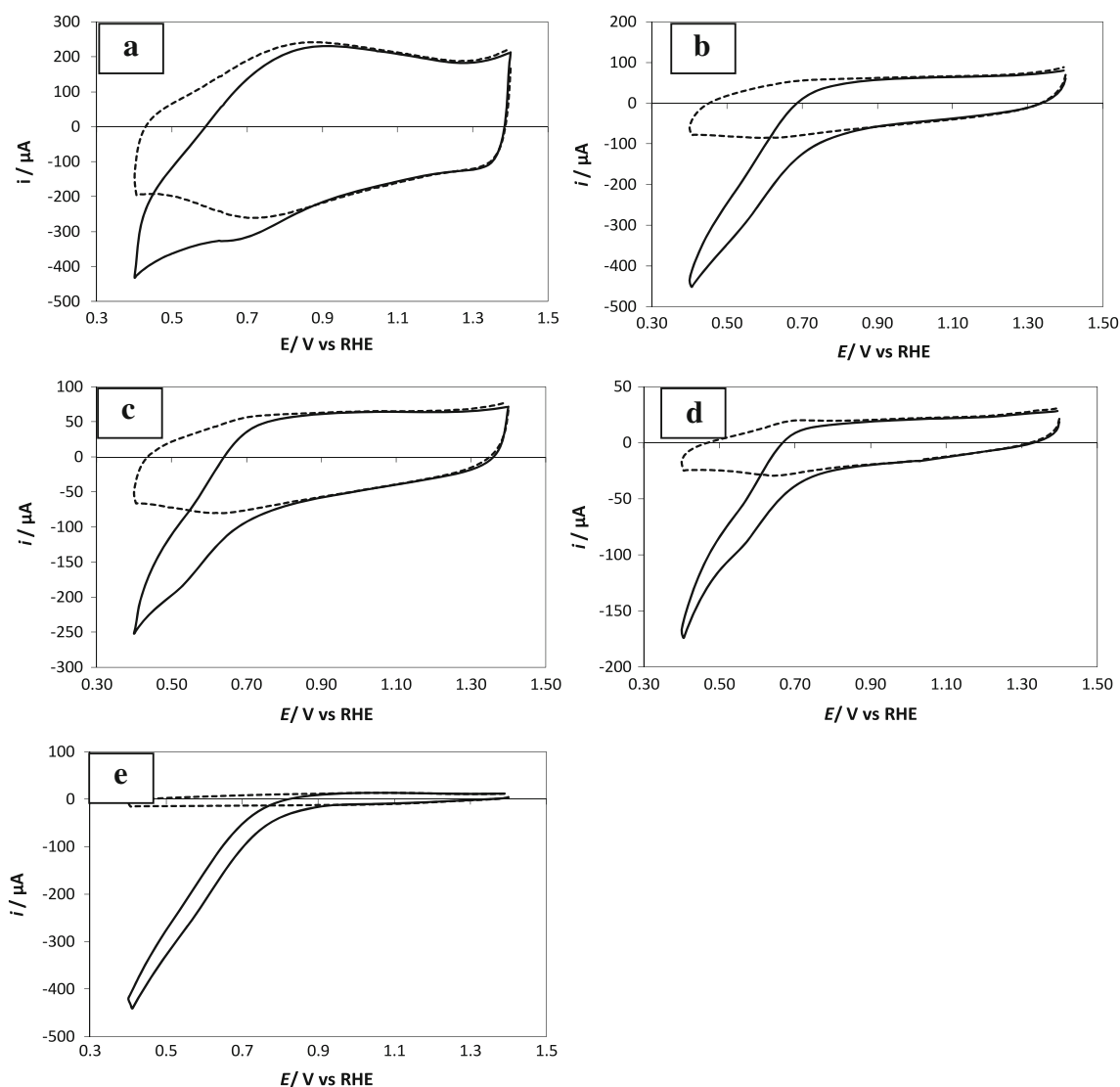


Fig. 6 CVs recorded on **a** $\text{SnO}_2 + \text{IrO}_2$ (0.15), **b** $\text{SnO}_2 + \text{IrO}_2$ (0.31), **c** $\text{SnO}_2 + \text{IrO}_2$ (0.50), **d** $\text{SnO}_2 + \text{IrO}_2$ (0.73), **e** pure IrO_2 , in N_2 -saturated (dashed line) or O_2 -saturated (solid line) 0.1 M NaOH. Scan rate 20 mV s^{-1} and rotation rate 2500 rpm

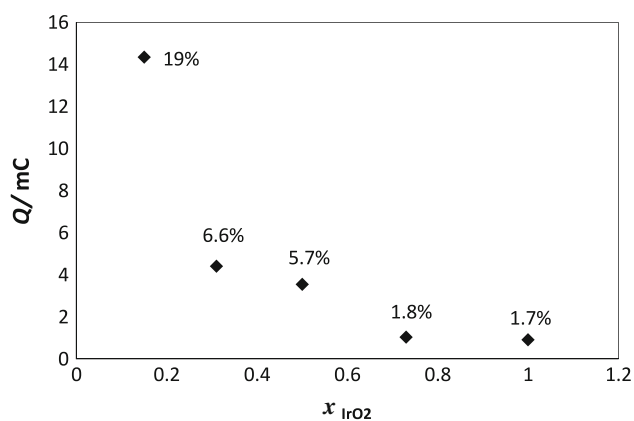


Fig. 7 Dependence of the voltammetric charge, Q (mC), on the IrO_2 mole fraction, x_{IrO_2} , in mixed tin–iridium oxides. Labels indicate the % of available sites

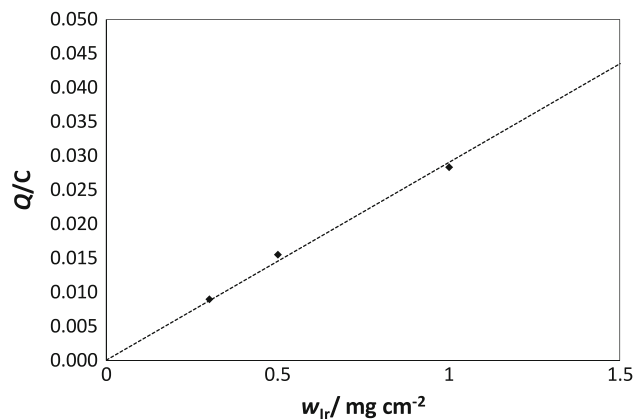


Fig. 8 Voltammetric charge at RDE electrodes modified with $\text{SnO}_2 + \text{IrO}_2$ (0.15) as a function of the Ir loading; experimental values—diamond, calculated straight line—dashed line

0.55 and 0.73, to invert again and reach its maximum value at pure IrO₂.

A similar trend is obtained at RRDE in SV experiments performed with the aim of determining both the kinetic features of the ORR and the fraction of hydrogen peroxide, if any, to quantify the ORR product distribution. The runs were carried out from 1.0 to 0.1 V (RHE) at 20 mV s⁻¹, while keeping the ring at 1.3 V, a potential positive enough to oxidize the hydrogen peroxide produced at the disk under mass transport control.

Figure 9 shows the quasi-steady-state disk and ring currents as functions of the potential applied to the disk, obtained by subtracting for each electrode the curve recorded in N₂-saturated electrolyte from that one in O₂-saturated electrolyte. The E_{ORR} values, obtained as described in Sect. 2, are very promising and only slightly dependent on mixture composition: 0.93 V SnO₂ + IrO₂ (0.15), 0.92 V SnO₂ + IrO₂ (0.31), 0.88 V SnO₂ + IrO₂ (0.50) and 0.90 V SnO₂ + IrO₂ (0.73). For what concerns the disk current profile, all materials present a similar shape. As expected, the disk current increases toward the less positive potentials, then exhibit a plateau in the range 0.40–0.65 V. The disk current trends resemble those previously observed by other groups in testing IrO₂ or RuO₂ materials [13–15]. Note that the disk current plateau corresponds to a broad maximum in the ring current indicating the potential window of maximum H₂O₂ production, as shown in Fig. 10 that represents the hydrogen peroxide percentage as calculated from Eq. 5 [31] starting from the ring and disk electrodes current values. We believe that the product distribution, together with the role of the two components in the reaction mechanism (see below), are at the basis of the disk current shape.

$$\% \text{H}_2\text{O}_2 = \frac{200(I_{\text{R}}/N)}{I_{\text{D}} + (I_{\text{R}}/N)} \quad (5)$$

The RRDE results, which point to the SnO₂ + IrO₂ (0.31) as the most effective electrocatalyst, comparable with pure IrO₂ in terms of oxygen reduction current and superior to it in terms of lower hydrogen peroxide formation, are in apparent contradiction with the outcomes from the Q values discussed previously. While in the case of OER the number of available sites is proportional to the Q values [30], this seems not to be the case for ORR. We suggest that, here, SnO₂ has a role in the overall ORR current: as reported previously [19, 20], SnO₂ conductivity exponentially increases toward less positive potentials (more than three order of magnitude from 1.4 to 0.4 V) up to the limiting case at which the electrons driven by the potentiostat can be directly injected into the SnO₂ conduction band, reaching a free motion condition. Hence the first ORR step, i.e. the dissociative chemisorption of

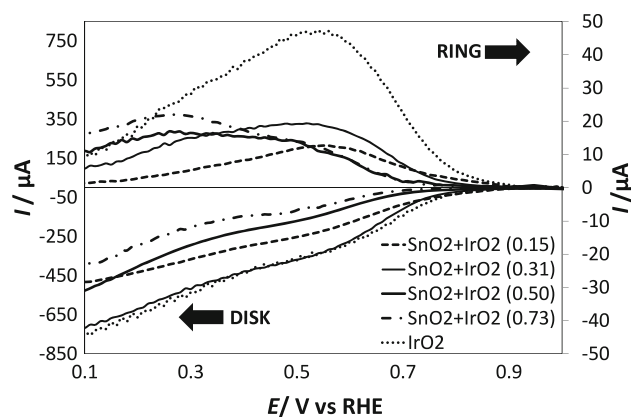


Fig. 9 Disk (bottom graph) and ring (upper graph) currents relevant to SVs recorded at 2500 rpm in 0.1 M NaOH

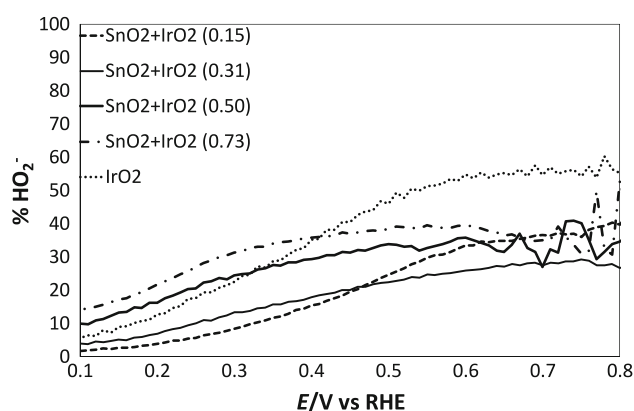


Fig. 10 Percentages of produced hydrogen peroxide as calculated by Eq. 5 starting from data collected in SV experiments

molecular oxygen, which is favored by the presence of easily oxidizable metal centers [32], would take advantage of the progressively increasing possibility for tin to participate to redox transitions. While IrO₂ would maintain its major role as the most active component, as envisaged by maximum activity recorded for both pure IrO₂ and for SnO₂ + IrO₂ (0.31), tin oxide, even at subsurface level, would promote the 4-electrons path and reduce the H₂O₂ formation. In fact, SnO₂ + IrO₂ (0.31) clearly presents the lower H₂O₂ production and can be safely ranked as the most promising material. It is not yet clear whether the 2-electrons pathway is simply hindered at SnO₂ + IrO₂ (0.31) or the catalytic power of the mixed oxide for H₂O₂ disproportionation is at the basis of the relatively low percentage of detected H₂O₂ at the ring while testing this material performances. Therefore, the role of SnO₂ in promoting the ORR while reducing the H₂O₂ production is mostly evident for an intermediate composition (0.31) and this is likely due to the optimal surface composition. In fact, as already evidenced [18], SnO₂–IrO₂ composites, obtained by impregnation and with a low-Ir content show

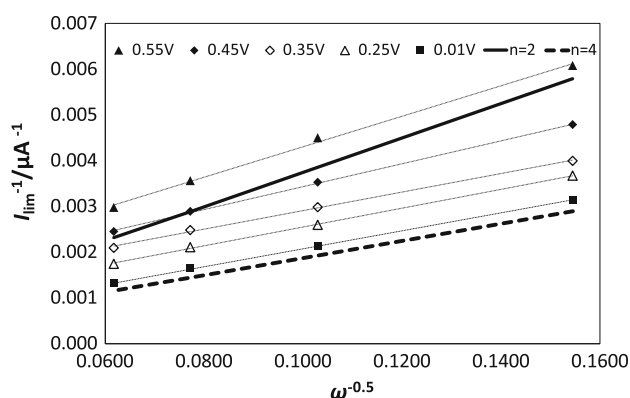


Fig. 11 Koutecky–Levich plots obtained from SV data recorded on sample $\text{SnO}_2 + \text{IrO}_2$ (0.31). The potential values to which the set of data and the relevant *straight lines* refer to are indicated in the legend. Note that the intercept at $\omega^{-0.5} \rightarrow 0$ corresponds to j_k^{-1}

an IrO_2 -enriched surface that covers a SnO_2 -doped core. This structural scheme is at the basis of high activity for both OER [17] and ORR.

As a general trend, all materials present a shift in the reaction path in dependence on the applied potential. This is evident in both Figs. 10 and 11, the latter representing Koutecky–Levich plots for sample $\text{SnO}_2 + \text{IrO}_2$ (0.31) at different disk potentials.

In particular, Fig. 11 collects the data recorded between 0.55 and 0.10 V (RHE), a range within which the number of exchanged electrons, n , increases until, at the less positive potentials, the amount of produced H_2O_2 is very low or even negligible.

3.2 Methanol tolerance of $\text{SnO}_2 + \text{IrO}_2$ (0.31)

The performance of the cathode material in a DAFC is often influenced by the presence of alcohol, which, fed to the anodic compartment, crosses the solid polymer

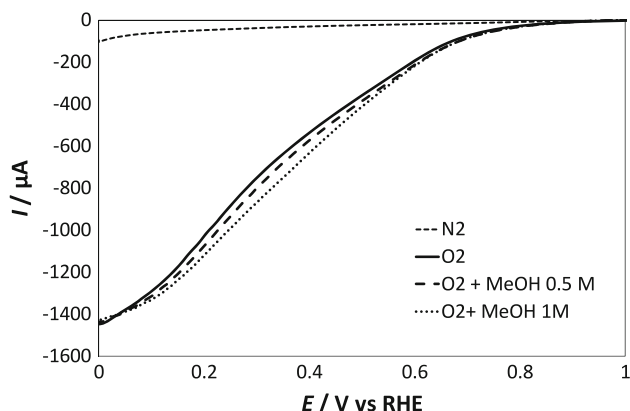


Fig. 12 SVs recorded on $\text{SnO}_2 + \text{IrO}_2$ (0.31) in the presence or absence of MeOH

electrolyte and directly oxidizes at positive electrode, short circuiting the cell and damaging the cathode catalytic layer. The best electrocatalysts should then exhibit a good “alcohol tolerance”, i.e., be inert to the direct chemical oxidation of the alcohol.

Figure 12 reports the influence of methanol on the SV curves obtained in O_2 -saturated NaOH 0.1 M in the case of the most promising material, i.e., $\text{SnO}_2 + \text{IrO}_2$ (0.31).

As can be observed, the electrocatalytic material shows an high oxygen reduction selectivity since the presence of methanol does not significantly modify the reduction current. This aspect is of great advantage in view of the application in DAFC.

4 Conclusions

In this work, the activity toward the ORR of $\text{SnO}_2 + \text{IrO}_2$ mixed oxides was studied in alkaline media by means of rotating (ring) disk electrodes. All powders were supported onto the glassy carbon disks thanks to thin layer of an anionic ionomer whose optimal amount was experimentally determined. The CV investigations performed in the absence of oxygen, in the pseudo-capacitive potential region, allow the determination of the fraction of electrocatalytic sites available for the water/proton/hydroxyl exchange between the oxide and the electrolyte solution and the concomitant electron transfers within the oxide matrix. The quasi-steady-state SV tests, extended from 1.1 to 0.1 V (RHE), evidence the superior behavior of both IrO_2 and $\text{SnO}_2 + \text{IrO}_2$ (0.31) for the ORR, when compared with the other $\text{SnO}_2 + \text{IrO}_2$ mixtures, highlighting at the same time a deep difference in the product distribution of the reaction, and more specifically in the formation of hydrogen peroxide, at least at the more positive potentials. These last results highlighted an important and unexpected role of SnO_2 that, together with a small percentage of IrO_2 , has a synergistic effect in promoting the ORR reducing the H_2O_2 production. This is likely due as easier dissociative chemisorption of molecular oxygen.

Acknowledgments Financial supports from the Italian Ministry of Education, University and Research (PRIN 2008N7CYL5), Fondazione Cariplo (2010-0506) and Università degli Studi di Milano (PUR 2009 Funds) are gratefully acknowledged.

References

1. Lamy C, Lima A, LeRhun V, Delime F, Countanceau C, Lèger JM (2002) Recent advances in the development of direct alcohol fuel cells (DAFC). *J Power Sources* 105:283–296
2. Tripkovic AV, Popovic KD, Grgur BN, Blizanac B, Ross PN, Markovic NM (2002) Methanol electrooxidation on supported Pt

- and PtRu catalysts in acid and alkaline solutions. *Electrochim Acta* 47:3707–3714. doi:[10.1016/S0013-4686\(02\)00340-7](https://doi.org/10.1016/S0013-4686(02)00340-7)
3. Scott K, Yua E, Vlachogiannopoulos G, Shivare M, Duteanu N (2008) Performance of a direct methanol alkaline membrane fuel cell. *J Power Sources* 175:452–457
 4. Blizanac BB, Ross PN, Markovic NM (2007) Oxygen electroreduction on Ag(1 1 1): the pH effect. *Electrochim Acta* 52:2264–2271. doi:[10.1016/j.electacta.2006.06.047](https://doi.org/10.1016/j.electacta.2006.06.047)
 5. Meng H, Jaouen F, Proietti E, Lefèvre M, Dodelet JP (2009) pH-effect on oxygen reduction activity of Fe-based electro-catalysts. *Electrochem Commun* 11(10):1986–1989. doi:[10.1016/j.elecom.2009.08.035](https://doi.org/10.1016/j.elecom.2009.08.035)
 6. Carrette L, Friedrich KA, Stimming U (2000) Fuel cells: principles, types, fuels, and applications. *ChemPhysChem* 1:162–193
 7. Wang Y, Zhang D, Liu H (2010) A study of the catalysis of cobalt hydroxide towards the oxygen reduction in alkaline media. *J Power Sources* 195:3135–3139. doi:[10.1016/j.jpowsour.2009.11.112](https://doi.org/10.1016/j.jpowsour.2009.11.112)
 8. Ye Y, Kuai L, Geng B (2012) A template-free route to a Fe_3O_4 - Co_3O_4 yolk-shell nanostructure as a noble-metal free electrocatalyst for ORR in alkaline media. *J Mater Chem* 22:19132–19138. doi:[10.1039/c2jm33893a](https://doi.org/10.1039/c2jm33893a)
 9. He Q, Yang X, Ren X, Koel BE, Ramaswamy N, Mukerjee S, Kostecki R (2011) A novel CuFe-based catalyst for the oxygen reduction reaction in alkaline media. *J Power Sources* 196:7404–7410. doi:[10.1016/j.jpowsour.2011.04.016](https://doi.org/10.1016/j.jpowsour.2011.04.016)
 10. Valim RB, Santos MC, Lanza MRV, Machado SAS, Lima FHB, Calegari ML (2012) Oxygen reduction reaction catalyzed by ε - MnO_2 : influence of the crystalline structure on the reaction mechanism. *Electrochim Acta*. doi:[10.1016/j.electacta.2012.08.075](https://doi.org/10.1016/j.electacta.2012.08.075)
 11. Olson TS, Pylypenko S, Atanasov P, Asazawa K, Yamada K, Tanaka H (2010) Anion-exchange membrane fuel cells: dual-site mechanism of oxygen reduction reaction in alkaline media on cobalt-polypyrrole electrocatalysts. *J Phys Chem C* 114:5049–5059. doi:[10.1021/jp910572g](https://doi.org/10.1021/jp910572g)
 12. Sun W, Hsu A, Chen R (2011) Carbon-supported tetragonal MnOOH catalysts for oxygen reduction reaction in alkaline media. *J Power Sources* 196:627–635. doi:[10.1016/j.jpowsour.2010.07.082](https://doi.org/10.1016/j.jpowsour.2010.07.082)
 13. Yoshinaga N, Sugimoto W, Takasu Y (2008) Oxygen reduction behavior of rutile-type iridium oxide in sulfuric acid solution. *Electrochim Acta* 54:566–574. doi:[10.1016/j.electacta.2008.07.020](https://doi.org/10.1016/j.electacta.2008.07.020)
 14. Takasu Y, Sugimoto W, Yoshitake M (2007) Developments of materials and evaluation methods for PEFCs. *Electrochemistry* 75:105–114
 15. Takasu Y, Yoshinaga N, Sugimoto W (2008) Oxygen reduction behavior of RuO_2/Ti , IrO_2/Ti and IrM (M: Ru, Mo, W, V) Ox/Ti binary oxide electrodes in a sulfuric acid solution. *Electrochem Commun* 10:668–672. doi:[10.1016/j.elecom.2008.02.014](https://doi.org/10.1016/j.elecom.2008.02.014)
 16. Changa CC, Wen TC, Yang CH (2009) Juang YD Influence of calcination temperature of IrO_2/Ti electrodes on oxygen reduction. *Mater Chem Phys* 115:93–97. doi:[10.1016/j.matchemphys.2008.11.015](https://doi.org/10.1016/j.matchemphys.2008.11.015)
 17. Minguzzi A, Locatelli C, Cappelletti G, Bianchi CL, Vertova A, Ardizzone S, Rondinini S (2012) Designing materials by means of the cavity-microelectrode: the introduction of the quantitative rapid screening toward a highly efficient catalyst for water oxidation. *J Mater Chem* 22:8896–8902. doi:[10.1039/C2JM15750K](https://doi.org/10.1039/C2JM15750K)
 18. Minguzzi A, Locatelli C, Cappelletti G, Scavini M, Vertova A, Ghigna P, Rondinini S (2012) IrO_2 -based disperse-phase electrocatalysts: a complementary study by means of the cavity-microelectrode and ex-situ X-ray absorption spectroscopy. *J Phys Chem A* 116:6497–6504. doi:[10.1021/jp212310v](https://doi.org/10.1021/jp212310v)
 19. Ardizzone S, Cappelletti G, Ionita M et al (2005) Low-temperature sol-gel nanocrystalline tin oxide integrated characterization of electrodes and particle obtained by a common path. *Electrochim Acta* 50:4419–4425. doi:[10.1016/j.electacta.2005.02.005](https://doi.org/10.1016/j.electacta.2005.02.005)
 20. Ionita M, Cappelletti G, Minguzzi A et al (2006) Bulk, surface and morphological features of nanostructured tin oxide by a controlled alkoxide-gel path. *J Nanopart Res* 8:653–660. doi:[10.1007/s11051-005-8383-8](https://doi.org/10.1007/s11051-005-8383-8)
 21. Ardizzone S, Bianchi CL, Borgese L, Cappelletti G, Locatelli C, Minguzzi A, Rondinini S, Vertova A, Ricci PC, Cannas C, Musinu A (2009) Physico-chemical characterization of IrO_2 - SnO_2 sol-gel nanopowders for electrochemical applications. *J Appl Electrochem* 39:2093–2105. doi:[10.1007/s10800-009-9895-1](https://doi.org/10.1007/s10800-009-9895-1)
 22. Locatelli C (2009) Multiphase, multifunctional micro- and nanostructured electrocatalytic materials for green chemistry: application to energy conversion and environmental protection. PhD Thesis
 23. Takenaka H, Torikai E, Kawami Y, Wakabayashi N (1982) Solid polymer electrolyte water electrolysis. *Int J Hydrogen Energy* 7:397–403
 24. Paulus UA, Schmidt TJ, Gasteiger HA, Behm RJ (2001) Oxygen reduction on a high-surface area Pt/Vulcan carbon catalyst: a thin-film rotating ring-disk electrode study. *J Electroanal Chem* 495:134–145
 25. Schmidt TJ, Gasteiger HA, Stäb GD, Urban PM, Kolb DM, Behm RJ (1998) Characterization of high-surface-area electrocatalysts using a rotating disk electrode configuration. *J Electrochem Soc* 145:2354–2358
 26. Minguzzi A, Fan FRF, Vertova A, Rondinini S, Bard AJ (2012) Dynamic potential-pH diagrams application to electrocatalysts for water oxidation. *Chem Sci* 3:217–229. doi:[10.1039/C1SC00516B](https://doi.org/10.1039/C1SC00516B)
 27. Ardizzone S, Bianchi CL, Cappelletti G et al (2006) Composite ternary SnO_2 - IrO_2 - Ta_2O_5 oxide electrocatalysts. *J Electroanal Chem* 589:160–166. doi:[10.1016/j.jelechem.2006.02.004](https://doi.org/10.1016/j.jelechem.2006.02.004)
 28. Ardizzone S, Carugati A, Trasatti S (1981) Properties of thermally prepared iridium dioxide electrodes. *J Electroanal Chem* 126:287–292
 29. Ardizzone S, Fregonara G, Trasatti S (1990) “Inner” and “outer” active surface of RuO_2 electrodes. *Electrochim Acta* 35:263–267
 30. Locatelli C, Minguzzi A, Vertova A, Cava P, Rondinini S (2011) Quantitative studies on electrode material properties by means of the cavity microelectrode. *Anal Chem* 83:2819–2823. doi:[10.1021/ac200286q](https://doi.org/10.1021/ac200286q)
 31. Miah MR, Ohsaka T (2009) Kinetics of oxygen reduction reaction at tin-adatoms-modified gold electrodes in acidic media. *Electrochim Acta* 54:5871–5876. doi:[10.1016/j.electacta.2009.05.045](https://doi.org/10.1016/j.electacta.2009.05.045)
 32. Fernandez JL, Walsh DA, Bard AJ (2005) Thermodynamic guidelines for the design of bimetallic catalysts for oxygen electroreduction and rapid screening by scanning electrochemical microscopy. *M-Co* (M: Pd, Ag, Au). *J Am Chem Soc* 127:357–365. doi:[10.1021/ja0449729](https://doi.org/10.1021/ja0449729)